

# Antarctic regional inversions using Elmer/Ice: methodology

Rupert Gladstone<sup>1</sup> and Yu Wang<sup>2</sup>

<sup>1</sup>Arctic Centre, University of Lapland, Rovaniemi, Finland

<sup>2</sup>College of Global Change and Earth System Science, Beijing Normal University, Beijing, China

**Correspondence:** Rupert Gladstone (RupertGladstone1972@gmail.com)

## 1 Introduction

This document describes simulations of the Pine Island Glacier (PIG) and the Lambert Amery Glacier System (LAGS) carried out using Elmer/Ice. This is a description of experiments that will feature in a forthcoming paper. It is made available as a methodology document in order to support other publications that use the outputs from these simulations.

## 2 Methodology

The Stokes-flow ice dynamic model Elmer/Ice (Gagliardini et al., 2013) was used for all simulation in the current study. Many different simulations are carried out in the current study, and these are grouped into experiments, as summarised in Fig. 1. Each simulation restarts from a previous simulation in the workflow, initialising using certain outputs from the previous simulation. Individual simulations in the current study are named *domain\_EX\_SM\_LX\_USBC\_BMB* where the name components are as given in Table 1.

Inversions are key to this study. We implement, using the adjoint method, inversions both for basal resistance (Gillet-Chaulet et al., 2012, 2016; Zhao et al., 2018; Seroussi et al., 2020) and for a viscosity enhancement factor (Sect. 2.3). Inversion methods in the current study follow the implementation in Elmer/Ice described by Gillet-Chaulet et al. (2012) except where stated otherwise.

### 2.1 Input data

Upper and lower ice surface elevation and bedrock elevation are from the BedMachine project (Morlighem et al., 2020).

For an initial estimate of basal resistance (specifically the parameter  $\beta$ ; see equation 2), we use output from an earlier whole-Antarctic inversion using Elmer/Ice (Gladstone

et al., 2019; Seroussi et al., 2020), interpolated onto the finer meshes used in the current study.

The initial 3D temperature field is from a whole-Antarctic multi-millennial spin up with the ice sheet model SICOPOLIS (Greve et al., 2020; Seroussi et al., 2020), interpolated onto the Elmer/Ice mesh.

The target dataset for the inversions presented in the current study consists of upper surface velocities observed using synthetic aperture radar interferometry from the MEaSUREs project (Rignot et al., 2017). These velocities were also used to generate a mesh refinement metric.

For the surface relaxation simulation in the current study, the basal mass balance under the ice shelf uses the Ice Sheet Model Intercomparison Project (ISMIP6) “local quadratic melting parameterisation” (Jourdain et al., 2020; Seroussi et al., 2020). For the upper surface mass balance, the 1995 to 2014 mean from the MAR model is used (Agosta et al., 2019).

For the simulations in which the 3D temperature field is solved for instead of prescribed, the spatial distribution of geothermal heat flux of Martos et al. (2017) is used under grounded ice. This is estimated from airborne magnetic data. The upper surface temperature is derived from a combination of in-situ measurements and satellite infrared observations (Comiso, 2000).

The PIG grounded catchment is delineated using ICEsat data (Zwally et al., 2012), with a manual adjustment to expand the catchment’s eastern boundary. The 2017 post-calving PIG ice front position was digitised from Sentinel 1 (Lea, 2018). The LAGS catchment and ice front position were provided through the initMIP project (Seroussi et al., 2019).

### 2.2 Mesh generation

The current study solves the Stokes equations on a 3D mesh using the finite element method (Gagliardini et al., 2013).

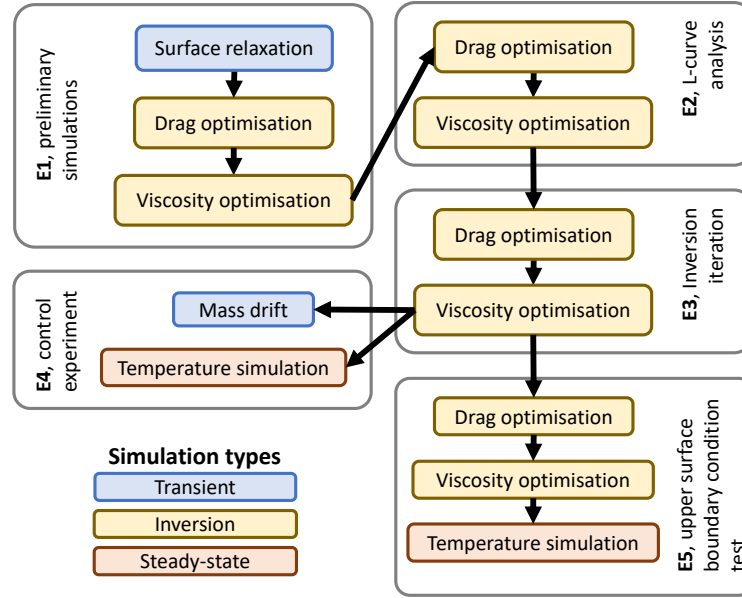


**Figure 1.** Overview of workflow for simulations implemented in the current study. Simulations are indicated in coloured boxes. Experiments 1 to 5 described in Sections 2.3 to 2.7 are indicated in grey outlined boxes. An experiment is a set of simulations. Black arrows indicate the use of the final model state from a simulation to initialise the following simulation.

**Table 1.** Summary of simulation naming convention.

Name part	Meaning	Possible values	Default (if not given)
<i>domain</i>	The domain on which this simulation is run	PIG or LAGS	Required
<i>EX</i>	Experiment number	From E1 to E5	Required
<i>SM</i>	Simulation mode	SR, IB, IV, Temp, Drift (Table 2)	Required
<i>LX</i>	Exponent of regularisation parameter, $\lambda$	From 1 ( $\lambda = 10^1$ ) to 8 ( $\lambda = 10^8$ )	As in Table 4
<i>USBC</i>	Upper surface boundary condition	ns, di, c1, c2, c3 (Sec. 2.7)	ns (no stress)
<i>BMB</i>	Basal mass balance	ISMIP6, Adusumilli	BMB not used

**Table 2.** Summary of simulation modes used in simulation naming.

Simulation mode	Meaning (described in)
SR	Surface relaxation (transient, Sec. 2.3)
IB	Inversion for basal drag (Sec. 2.3)
IV	Inversion for viscosity enhancement (Sec. 2.3)
Temp	Steady temperature simulation (Sec. 2.6)
Drift	Drift estimation (transient, Sec. 2.6)

The 3D mesh is extruded from an unstructured 2D footprint of triangular elements, such that all bulk elements are triangular prisms.

The footprint mesh is created using Gmsh (Geuzaine and Remacle, 2009) and the domain boundaries (Sec. 2.1) to generate an approximately uniform mesh of irregular triangular elements. This is then refined using Mmg (Dapogny et al., 2014). The refinement metric uses both observed velocity and ice thickness to determine refinement (finer resolution is used where gradients in velocity and thickness are greatest). Upper and lower limits to element size are also applied constrained by distance from both grounding line and domain boundary.

The 2D footprint mesh is then extruded vertically. The vertically extruded structure is maintained throughout the simulations such that in transient simulations the lateral domain boundaries (including the ice fronts) remain vertical while the upper and lower (in the case of floating ice) surfaces evolve.

The LAGS 2D footprint mesh is constrained to have a minimum element size of 2km and maximum element size of 15km. The maximum element size at the fast flowing regions of the grounding line is 2.5km. The maximum element size in the ice shelf is 4km. The mesh is extruded into 20 layers in the vertical for a total of approximately 1.0 million bulk elements.

The PIG 2D footprint mesh is constrained to have a minimum element size of 0.6km and maximum element size of 11km. The maximum element size at the fast flowing regions of the grounding line is 0.7km. The maximum element size in the ice shelf is 1.7km. The mesh is extruded into 15 layers in the vertical for a total of approximately 1.1 million bulk elements.

### 2.3 Experiment 1: preliminary simulations

The aim of the preliminary simulations is to provide a sane starting point for the L-curve analysis. This experiment comprises three simulations: a short transient surface relaxation simulation followed by an optimisation simulation for basal drag and finally an optimisation for viscosity enhancement.

#### 2.3.1 Surface relaxation

The surface relaxation is run for 40 timesteps with increasing timestep size,  $\Delta t$ , given by

$$\Delta t(n) = 10^{-5} \times 1.2^n, \quad (1)$$

where  $n$  is the number of timesteps. This approximates to a total run time of one month, allowing adjustment of the floating ice shelf toward dynamic equilibrium without significantly altering the ice geometry. The main purpose of this simulation is to allow an initial adjustment of the ice shelf. This is required because our initial state imposes floatation, whereas the Stokes solution is not in general at floatation, especially close to the grounding line, hence strong initial vertical adjustments occur during the surface relaxation in the portion of the shelf close to the grounding line.

The Amery surface relaxation, simulation LAGS\_E1\_SR\_ISMIP6, exhibited very high velocities close to an ice rise in the later stages, hence the geometry from timestep 15 (corresponding to a run time of 0.01 months) is used for subsequent simulations (specifically as a starting point for LAGS\_E1\_IB).

This surface relaxation is a standard transient simulation following Gagliardini et al. (2013). Ocean pressure (calculated using depth relative to sea level and the densities in Table 3) is imposed under the ice shelf and at the ice front where it is below sea level (Gagliardini et al., 2013). Ocean pressure is also imposed in the same way in the other preliminary simulations (described below) and in experiments 2 and 3 (Sec. 2.4 and 2.5). Estimates for upper and lower surface mass balance (described in Sec. 2.1) are applied on the upper surface everywhere and on the lower surface of the ice

**Table 3.** Physical constants

Parameter	Value
Ocean water density, $\rho_o$	$1027 \text{kgm}^{-3}$
Ice density, $\rho_i$	$917 \text{kgm}^{-3}$

shelf (normal velocity is set to zero at the lower surface of grounded ice), though the simulation is too short for these to have a large effect. The grounding line is not allowed to move during this surface relaxation.

#### 2.3.2 Inversion for basal drag

The drag inversions optimise a drag exponent,  $\beta$ , in a linear sliding relation given by

$$\tau_b = 10^\beta u_b, \quad (2)$$

where  $\tau_b$  is basal resistance and  $u_b$  is sliding speed. The implementation is as described by Gillet-Chaulet et al. (2012).

The inversions make use of Tikhonov regularisation (as in Gillet-Chaulet et al. (2012); see also Sec. 2.4). Two separate regularisation parameters,  $\lambda_\beta$  and  $\lambda_\eta$ , are used for the drag inversions and viscosity enhancement factor inversions (described below) respectively. For the preliminary simulations, we set  $\lambda_\beta = \lambda_\eta = 10^4$ .

#### 2.3.3 Inversion for viscosity enhancement

The final simulation of the preliminary experiment is for a viscosity enhancement factor,  $E_\eta$ . This is defined such that equation 4 from Gagliardini et al. (2013), which determines the effective viscosity,  $\eta$ , becomes

$$\eta = \frac{E_\eta^2}{2} A^{\frac{-1}{n}} \dot{\epsilon}_e^{\frac{(1-n)}{n}}, \quad (3)$$

where  $\dot{\epsilon}_e$  is the second invariant of the strain rate,  $n$  is the exponent in Glen's law, and  $A$  is a rheological parameter, dependant, via an Arrhenius law, on ice temperature relative to the pressure melting point.  $E_\eta$  is initialised to a spatially uniform value of 1, i.e. no enhancement. Lower numbers indicate more rapid deformation and higher numbers indicate stiffer ice.

Equation 3, together with equation 4 from Gagliardini et al. (2013), imply the following relationship between our viscosity enhancement factor,  $E_\eta$ , and the more commonly used flow enhancement factor  $E$  (e.g. Ma et al. (2010); Gagliardini et al. (2013)).

$$E = E_\eta^{-6} \quad (4)$$

The approach is implemented in a combination of 2 and 3 dimensions. Each iteration of the optimisation process includes the following. The ice flow is solved in 3D. The cost

**Table 4.** Chosen regularisation after L-curve analysis.

Domain	$\lambda_\beta$	$\lambda_\eta$
PIG	$10^3$	$10^4$
LAGS	$10^3$	$10^4$

function, and its gradients, are also calculated in the full 3D ice body. These are summed in the vertical (facilitated by the vertically extruded mesh, Sect 2.2) and the actual optimisation procedure is carried out in 2D, similar to the optimisation for basal resistance. The optimised 2D  $E_\eta$  is then projected in the vertical to all nodes. Thus  $\eta$  exhibits vertical variation through the temperature dependence of A, but the optimisation of  $E_\eta$  only impacts on the horizontal distribution of  $\eta$  (i.e.  $E_\eta$  is uniform in the vertical direction). This optimisation is carried out with regularisation (Sect. 2.4), setting  $\lambda_\eta = 10^4$ .

The end point of this experiment is a model state with a plausible 3D velocity field and plausible distributions for  $E_\eta$  and  $\beta$ .

## 2.4 Experiment 2: L-curve analysis

Regularisation in the current study follows Gillet-Chaulet et al. (2012), in which a Tikhonov regularisation term,  $J_{reg}$ , penalises spatial derivatives of the parameter being optimised ( $\beta$  or  $E_\eta$ ). The aim is to avoid overfitting to noisy observational data. The total cost function,  $J_{tot}$ , is now the sum of misfit,  $J_0$ , and weighted regularisation term, i.e.

$$J_{tot} = J_0 + \lambda_\beta J_{reg} \quad (5)$$

for the drag inversion ( $\lambda_\beta$  would be replaced by  $\lambda_\eta$  for the viscosity enhancement factor inversion). For the drag inversion, we carry out an L-curve analysis, in which 8 inversion simulations are carried out for different values of  $\lambda_\beta$ , increasing from 10 to  $10^8$  by factor 10 each time. For the L-curve itself,  $J_{reg}$  is plotted against  $J_0$  in log-log space. The L-curve is a graphical tool for displaying the trade-off between the size of a regularized solution and its fit to the given data, as  $\lambda_\beta$  varies. We use this to choose a value of  $\lambda_\beta$  to use in all following simulations.

This process is then repeated for the viscosity enhancement factor simulations, using as input the  $\beta$  distribution from the inversion simulation with our preferred  $\lambda_\beta$ , resulting in a value for  $\lambda_\eta$ .

The end point of experiment 2 should represent a good estimate for the spatial distributions of  $\beta$  and  $E_\eta$ , and gives  $\lambda_\beta$  and  $\lambda_\eta$  values to be used in further inversion simulations. The results of the L-curve analysis will be described in Sect. 3. For now we note that values given in Table 4 are chosen for use in the following inversions (Sect. 2.5).

## 2.5 Experiment 3: inversion iteration

Given that our drag and viscosity enhancement inversions are carried out sequentially,  $\beta$  and  $E_\eta$  can influence each other only as inputs at the start of a simulation. Future studies will aim to optimise both fields together in one simulation, but the current study allows some limited interaction by implementing an additional  $\beta$  and  $E_\eta$  inversion (in that order) after the L-curve analysis, using the same  $\lambda_\beta$  and  $\lambda_\eta$  values determined through the L-curve analysis (Table 4).

The end point of experiment 3 represents our current best estimate for the spatial distributions of  $\beta$  and  $E_\eta$  for use in further simulations and analyses.

## 2.6 Experiment 4: control experiment

The control experiment takes the final state from the optimisation procedures and uses this to calculate a steady state temperature field (simulations PIG\_E4\_Temp and LAGS\_E4\_Temp) and a mass drift based on a short transient simulation (simulations PIG\_E4\_Drift and LAGS\_E4\_Drift). The motivation is to analyse the applicability of the optimised model state to further simulations that may be used, for example, to quantify longer term transient change, to investigate thermodynamics, or to drive a sub-glacial hydrology model.

The temperature simulations follow the method described by Gagliardini et al. (2013) and incorporate heat generated by internal deformation, a Dirichlet boundary condition at the upper surface, and both friction heat due to sliding and geothermal heat at the bed, as in Zhao et al. (2018); Gladstone et al. (2014). The upper surface temperatures and geothermal heat flux data are described in Sect. 2.1. The ice velocities are taken from simulations PIG\_E3\_IV and LAGS\_E3\_IV.

The drift simulations are run for 4a with a timestep size of 0.05a using the same forcing and boundary conditions as the surface relaxation (simulations PIG\_E1\_SR\_ISMIP6 and LAGS\_E1\_SR\_ISMIP6) except that the optimised drag coefficient and viscosity enhancement factor are used and the grounding line is allowed to evolve.

## 2.7 Experiment 5: impact of upper surface boundary conditions

The sparse nature of observations of bedrock elevation beneath ice sheets can lead to large errors in estimates of the horizontal flux divergence, whether calculated directly from observations or by ice sheet modelling (Seroussi et al., 2011). Mass conservation methods help to improve accuracy of bedrock elevation, but local errors over 100m may still occur (Morlighem et al., 2020). An artificially noisy flux divergence field can cause significant non-physical advection into and out of the upper surface of the ice, which impacts on the simulated 3D ice temperatures (Sect. 2.6). Controlling

**Table 5.** Coefficients used for resistance upper surface boundary condition.

Label	$C$	$u^*$
c1	50 MPa a m <sup>-1</sup>	50 ma <sup>-1</sup>
c2	100 MPa a m <sup>-1</sup>	10 ma <sup>-1</sup>
c3	50 MPa a m <sup>-1</sup>	500 ma <sup>-1</sup>

for flux divergence when carrying out inversions by penalising non-zero values in the cost function can improve inversions when optimising the bedrock topography itself (Mosbeux et al., 2016). In the current study we constrain horizontal flux divergence by implementing several alternative boundary conditions for the upper surface normal velocity.

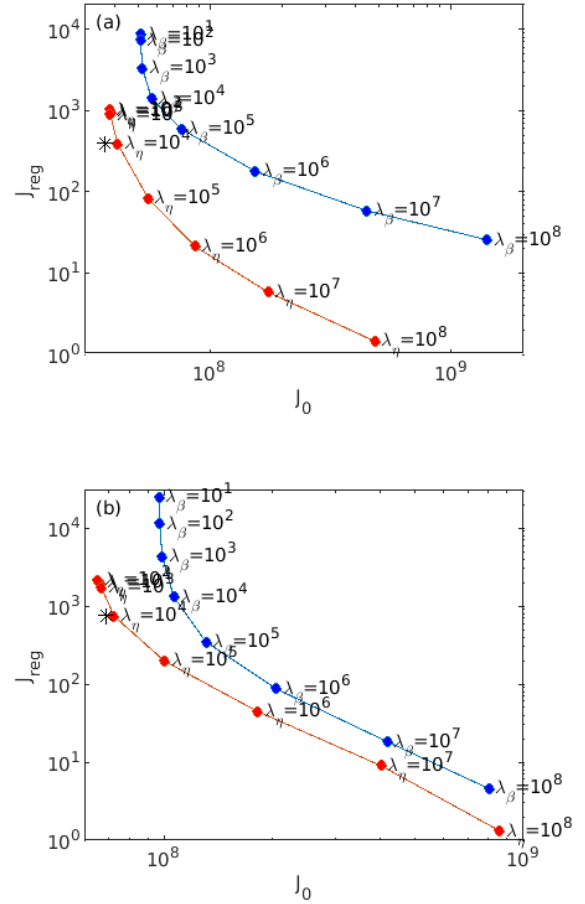
Firstly, as in experiments 1 to 4, a zero normal stress condition is used (henceforth “ns” for “no stress”, Table 1). Secondly, a Dirichlet condition is used, setting the normal component of the model velocity at the upper surface equal to a reference surface mass balance (henceforth “di”, Table 1; see Sect. 2.1 and Agosta et al. (2019) for surface mass balance). Thirdly, a non-zero resistance,  $\tau_r$ , is applied in the direction normal to the upper surface (henceforth “c1”, “c2” and “c3”, Tables 1 and 5):

$$\tau_r = -\mathbf{u} \cdot \mathbf{n}_s C \left[ 1 - \tanh \left( \frac{\|\mathbf{u}_{obs}\|}{u^*} \right) \right] \quad (6)$$

where  $\mathbf{u}$  is the modelled velocity,  $\mathbf{n}_s$  is the outward unit normal vector at the ice upper surface,  $C$  is a resistance coefficient,  $u^*$  is a reference speed, and  $\|\mathbf{u}_{obs}\|$  is the magnitude of the horizontal upper surface velocity from observations. This formulation imposes a stronger constraint on upper surface normal velocity in regions where horizontal observed flow speeds are higher.

For all simulations in experiment 5, a Dirichlet condition is applied at the lower surface of the ice shelf, setting the lower surface normal velocity equal in magnitude to an observationally based basal mass balance estimate, calculated using flux divergence in the ice and the steady state assumption (Adusumilli et al., 2020). Positive outward (i.e. approximately downward) corresponds to melt and negative outward corresponds to accretion. This choice of boundary condition is equivalent to assuming that the current ice geometry is in steady state with the given basal mass balance.

The optimisations of experiment 3, and the temperature simulation of experiment 4, are repeated for each upper surface BC described above, and the Dirichlet lower surface BC described above, using regularisation as in Table 4. The process is initialised using the final model state from experiment 3. The dependencies are shown in Fig. 1. Experiment 5 is carried out for the LAGS domain and not for the PIG domain.


**Figure 2.** L-curves from experiment 2. Regularisation term,  $J_{reg}$ , vs misfit,  $J_0$ , is shown for (a) PIG and (b) LAGS. The L-curves for the drag inversions are shown in blue and for the viscosity inversions in red. The asterisks show the final state of experiment 3.

### 3 L-curve analysis

Varying the regularisation parameter  $\lambda$  is commonly assessed through an “L-curve” analysis, seeking a compromise between over smoothing due to too much regularisation and over fitting to noisy data.

The L-curve is an aid in choosing an appropriate regularization parameter for the given data.

The L-curve is shown in Fig. 2.

## References

- Adusumilli, S., Fricker, H., Medley, B., Padman, L., and Siegfried, M.: Interannual variations in meltwater input to the Southern Ocean from Antarctic ice shelves., *Nat. Geosci.*, 13, 616–620, <https://doi.org/10.1038/s41561-020-0616-z>, <https://doi.org/10.1038/s41561-020-0616-z>, 2020.
- Agosta, C., Amory, C., Kittel, C., Orsi, A., Favier, V., Gallée, H., van den Broeke, M. R., Lenaerts, J. T. M., van Wessem, J. M., van de Berg, W. J., and Fettweis, X.: Estimation of the Antarctic surface mass balance using the regional climate model MAR (1979–2015) and identification of dominant processes, *The Cryosphere*, 13, 281–296, <https://doi.org/10.5194/tc-13-281-2019>, <https://tc.copernicus.org/articles/13/281/2019/>, 2019.
- Comiso, J. C.: Variability and Trends in Antarctic Surface Temperatures from In Situ and Satellite Infrared Measurements, *Journal of Climate*, 13, 1674 – 1696, [https://doi.org/10.1175/1520-0442\(2000\)013<1674:VATIAS>2.0.CO;2](https://doi.org/10.1175/1520-0442(2000)013<1674:VATIAS>2.0.CO;2), [https://journals.ametsoc.org/view/journals/clim/13/10/1520-0442\\_2000\\_013\\_1674\\_vatias\\_2.0.co\\_2.xml](https://journals.ametsoc.org/view/journals/clim/13/10/1520-0442_2000_013_1674_vatias_2.0.co_2.xml), 2000.
- Dapogny, C., Dobrzynski, C., and Frey, P.: Three-dimensional adaptive domain remeshing, implicit domain meshing, and applications to free and moving boundary problems, *Journal of Computational Physics*, 262, 358–378, <https://doi.org/https://doi.org/10.1016/j.jcp.2014.01.005>, <https://www.sciencedirect.com/science/article/pii/S0021999114000266>, 2014.
- Gagliardini, O., Zwinger, T., Gillet-Chaulet, F., Durand, G., Favier, L., de Fleurian, B., Greve, R., Malinen, M., Martín, C., Råback, P., Ruokolainen, J., Sacchetti, M., Schäfer, M., Seddik, H., and Thies, J.: Capabilities and performance of Elmer/Ice, a new-generation ice sheet model, *Geoscientific Model Development*, 6, 1299–1318, <https://doi.org/10.5194/gmd-6-1299-2013>, <https://www.geosci-model-dev.net/6/1299/2013/>, 2013.
- Geuzaine, C. and Remacle, J.-F.: Gmsh: A 3-D finite element mesh generator with built-in pre- and post-processing facilities, *International Journal for Numerical Methods in Engineering*, 79, 1309–1331, <https://doi.org/10.1002/nme.2579>, <http://dx.doi.org/10.1002/nme.2579>, 2009.
- Gillet-Chaulet, F., Gagliardini, O., Seddik, H., Nodet, M., Durand, G., Ritz, C., Zwinger, T., Greve, R., and Vaughan, D. G.: Greenland ice sheet contribution to sea-level rise from a new-generation ice-sheet model, *The Cryosphere*, 6, 1561–1576, <https://doi.org/10.5194/tc-6-1561-2012>, 2012.
- Gillet-Chaulet, F., Durand, G., Gagliardini, O., Mosbeux, C., Mouginot, J., Rémy, F., and Ritz, C.: Assimilation of surface velocities acquired between 1996 and 2010 to constrain the form of the basal friction law under Pine Island Glacier, *Geophysical Research Letters*, 43, 10,311–10,321, <https://doi.org/10.1002/2016GL069937>, <https://agupubs.onlinelibrary.wiley.com/doi/abs/10.1002/2016GL069937>, 2016.
- Gladstone, R., Schäfer, M., Zwinger, T., Gong, Y., Strozzii, T., Mottram, R., Boberg, F., and Moore, J. C.: Importance of basal processes in simulations of a surging Svalbard outlet glacier, *The Cryosphere*, 8, 1393–1405, <https://doi.org/10.5194/tc-8-1393-2014>, <http://www.the-cryosphere.net/8/1393/2014/>, 2014.
- Gladstone, R., Zhao, C., and Zwinger, T.: ISMIP6 Projections-Antarctica read me file, <https://doi.org/10.5281/zenodo.3484635>, 2019.
- Greve, R., Calov, R., Obase, T., Saito, F., Tsutaki, S., and Abe-Ouchi, A.: ISMIP6 future projections for the Antarctic ice sheet with the model SICOPOLIS, <https://doi.org/10.5281/zenodo.4035932>, funding acknowledgements: Japan Society for the Promotion of Science (JSPS) KAKENHI grant Nos. JP16H02224, JP17H06104 and JP17H06323. PalMod project (PalMod 1.1 and 1.3 with grants 01LP1502C and 01LP1504D) of the German Federal Ministry of Education and Research (BMBF), 2020.
- Jourdain, N. C., Asay-Davis, X., Hattermann, T., Straneo, F., Seroussi, H., Little, C. M., and Nowicki, S.: A protocol for calculating basal melt rates in the ISMIP6 Antarctic ice sheet projections, *The Cryosphere*, 14, 3111–3134, <https://doi.org/10.5194/tc-14-3111-2020>, <https://tc.copernicus.org/articles/14/3111/2020/>, 2020.
- Lea, J. M.: The Google Earth Engine Digitisation Tool (GEEDiT) and the Margin change Quantification Tool (MaQiT) – simple tools for the rapid mapping and quantification of changing Earth surface margins, *Earth Surface Dynamics*, 6, 551–561, <https://doi.org/10.5194/esurf-6-551-2018>, <https://esurf.copernicus.org/articles/6/551/2018/>, 2018.
- Ma, Y., Gagliardini, O., Ritz, C., Gillet-Chaulet, F., Durand, G., and Montagnat, M.: Enhancement factors for grounded ice and ice shelves inferred from an anisotropic ice-flow model, *Journal of Glaciology*, 56, 805–812, <https://doi.org/10.3189/002214310794457209>, 2010.
- Martos, Y. M., Catalán, M., Jordan, T. A., Golynsky, A., Golynsky, D., Eagles, G., and Vaughan, D. G.: Heat Flux Distribution of Antarctica Unveiled, *Geophysical Research Letters*, 44, 11,417–11,426, <https://doi.org/https://doi.org/10.1002/2017GL075609>, <https://agupubs.onlinelibrary.wiley.com/doi/abs/10.1002/2017GL075609>, 2017.
- Morlighem, M., Rignot, E., and Binder, T.: Deep glacial troughs and stabilizing ridges unveiled beneath the margins of the Antarctic ice sheet., *Nat. Geosci.*, 13, 132–137, <https://doi.org/https://doi.org/10.1038/s41561-019-0510-8>, 2020.
- Mosbeux, C., Gillet-Chaulet, F., and Gagliardini, O.: Comparison of adjoint and nudging methods to initialise ice sheet model basal conditions, *Geoscientific Model Development*, 9, 2549–2562, <https://doi.org/10.5194/gmd-9-2549-2016>, <https://gmd.copernicus.org/articles/9/2549/2016/>, 2016.
- Rignot, E., Mouginot, J., and Scheuchl, B.: MEASUREs InSAR-Based Antarctica Ice Velocity Map, Version 2., <https://doi.org/10.5067/D7GK8F5J8M8R>, <https://doi.org/10.5067/D7GK8F5J8M8R>, 2017.
- Seroussi, H., Morlighem, M., Rignot, E., Larour, E., Aubry, D., Ben Dhia, H., and Kristensen, S. S.: Ice flux divergence anomalies on 79north Glacier, Greenland, *Geophysical Research Letters*, 38, <https://doi.org/https://doi.org/10.1029/2011GL047338>, <https://agupubs.onlinelibrary.wiley.com/doi/abs/10.1029/2011GL047338>, 2011.
- Seroussi, H., Nowicki, S., Simon, E., Abe-Ouchi, A., Albrecht, T., Brondex, J., Cornford, S., Dumas, C., Gillet-Chaulet, F., Goelzer, H., Gollledge, N. R., Gregory, J. M., Greve, R., Hoffman, M. J., Humbert, A., Huybrechts, P., Kleiner, T., Larour, E., Leguy, G., Lipscomb, W. H., Lowry, D., Mengel, M., Morlighem, M., Pattyn, F., Payne, A. J., Pollard, D., Price, S. F., Quiquet, A., Reerink, T. J., Reese, R., Rodehacke, C. B., Schlegel, N.-J.,

- Shepherd, A., Sun, S., Sutter, J., Van Breedam, J., van de Wal, R. S. W., Winkelmann, R., and Zhang, T.: initMIP-Antarctica: an ice sheet model initialization experiment of ISMIP6, *The Cryosphere*, 13, 1441–1471, <https://doi.org/10.5194/tc-13-1441-2019>, <https://tc.copernicus.org/articles/13/1441/2019/>, 2019.
- 5 Seroussi, H., Nowicki, S., Payne, A. J., Goelzer, H., Lipscomb, W. H., Abe-Ouchi, A., Agosta, C., Albrecht, T., Asay-Davis, X., Barthel, A., Calov, R., Cullather, R., Dumas, C., Galton-Fenzi, B. K., Gladstone, R., Golledge, N. R., Gregory, J. M.,  
10 Greve, R., Hattermann, T., Hoffman, M. J., Humbert, A., Huybrechts, P., Jourdain, N. C., Kleiner, T., Larour, E., Leguy, G. R., Lowry, D. P., Little, C. M., Morlighem, M., Pattyn, F., Pelle, T., Price, S. F., Quiquet, A., Reese, R., Schlegel, N.-J., Shepherd, A., Simon, E., Smith, R. S., Straneo, F., Sun, S., Trusel, L. D., Van Breedam, J., van de Wal, R. S. W.,  
15 Winkelmann, R., Zhao, C., Zhang, T., and Zwinger, T.: ISMIP6 Antarctica: a multi-model ensemble of the Antarctic ice sheet evolution over the 21st century, *The Cryosphere*, 14, 3033–3070, <https://doi.org/10.5194/tc-14-3033-2020>, <https://tc.copernicus.org/articles/14/3033/2020/>, 2020.
- 20 Zhao, C., Gladstone, R. M., Warner, R. C., King, M. A., Zwinger, T., and Morlighem, M.: Basal friction of Fleming Glacier, Antarctica – Part 1: Sensitivity of inversion to temperature and bedrock uncertainty, *The Cryosphere*, 12, 2637–2652, <https://doi.org/10.5194/tc-12-2637-2018>, <https://www.the-cryosphere.net/12/2637/2018/>, 2018.
- 25 Zwally, H. J., Giovinetto, M. B., Beckley, M. A., and Saba, J. L.: Antarctic and Greenland drainage systems, GSFC Cryospheric Sciences Laboratory, 2012.